

Mei Feng<sup>1</sup>  
Jaime Gonzalez  
James A. Olson

Pulp and Paper Centre and Department of  
Mechanical Engineering, The University of British  
Columbia, 2385 East Mall, Vancouver BC,  
Canada, V6T 1Z4

**Carl Ollivier-Gooch**  
Department of Mechanical Engineering,  
The University of British Columbia,  
2324 Main Mall, Vancouver BC,  
Canada, V6T 1C4

**Robert W. Gooding**  
Advanced Fiber Technologies (AFT) Inc.,  
Montreal QC, Canada, H4A 1G2

# Numerical Simulation and Experimental Measurement of Pressure Pulses Produced by a Pulp Screen Foil Rotor

*Pressure screening is an efficient means of removing various contaminants that degrade the appearance and strength of paper. A critical component of a screen is the rotor, which induces a tangential velocity to the suspension and produces pressure pulses to keep the screen apertures clear. To understand the effect of key design and operating variables for a NACA foil rotor, a computational fluid dynamic (CFD) simulation was developed using FLUENT, and the results were compared to experimental measurements. Comparing the pressure pulses obtained through CFD to experimental measurements over a wide range of foil tip speeds, clearances, angles of attack, and foil cambers, general trends of the pressure pulses were similar, but the overall computed values were 40% smaller than the measured values. The pressure pulse peak was found to increase linearly with the square of tip speed for all the angles of attack studied. The maximum magnitudes of negative pressure pulse occurred for the NACA 0012 and 4312 foils at a 5 deg angle of attack and for the NACA 8312 foil at 0 deg. The stall angle of attack was found to be ~5 deg for NACA 8312, ~10 deg for NACA 4312, and ~15 deg for NACA 0012. The positive pressure peak near the leading edge of the foil was eliminated for foils operating at a positive angle of attack. The magnitude of the negative pressure coefficient peak increased as clearance decreased. Increased camber increases both the magnitude and width of the negative pressure pulse. [DOI: 10.1115/1.1881672]*

## Introduction

Pulp screens are used in virtually all pulp and paper operations worldwide. Pressure screening is the most industrially effective means of removing oversized contaminants that can degrade the appearance and strength of paper. Pressure screens are increasingly used to fractionate fibers by length so that the long or short fiber streams can be processed separately or used in high-value paper grades. For these reasons, pressure screens are assuming a special importance in the production of mechanical and recycled pulps, as well as for the manufacture of high-quality mechanical printing papers.

Pulp screens divide a contaminated feed flow into an accept stream of clean pulp and a reject stream laden with contaminants. During screening, the pulp and contaminants typically enter the screening zone tangentially. The pulp suspension flows between a rotor and the inlet side of a cylindrical screen. The fibers flow through the apertures in the screen cylinder and exit through the accept port. The oversized particles and a fraction of the long fibers are retained by the screen cylinder and travel down the annulus, leaving the screen through the reject port. To prevent the apertures from becoming plugged by the fibers, foils are passed over the feed side of the screen surface to create negative pressure pulses that backflush the apertures. The screen rotor comprises the foils, or some other pulse-inducing hydrodynamic elements, and the support structure.

The rotor plays a critical role in screen operation. Despite various differences in rotor design, all rotors serve two main functions. One function is to accelerate the pulp suspension on the

feed side of the screen to a high tangential velocity. This induces turbulence at the surface of the screen plate, which mixes the suspension and keeps the pulp fluidized. The second, and more important, function is to create a negative pressure pulse that backflushes the screen apertures, clearing any fiber accumulations and preventing plugging of the apertures.

The principal measures of screen performance are (i) contaminant removal efficiency, defined as the mass percentage of contaminants leaving the screen through the reject port relative to that entering the screen; (ii) capacity, the maximum mass flow rate of pulp in the accept stream; (iii) power consumption, the power consumed by the rotor normalized by the accept mass flow rate of fibers; and (iv) reject rate, the mass flow of fibers rejected with the contaminants. Achieving high capacity and high efficiency with reduced power consumption at a low reject rate is the goal of an optimal screen design.

Although rotor design is critical in determining pulp screen performance, the mechanism of pressure pulse generation and the factors that affect the magnitude and shape of the pressure pulse are not well understood. To better understand the critical rotor design factors affecting screen performance, computational fluid dynamics (CFD) was used to analyze the complex flow created by the rotor. In particular, this study considered how the key design and operating variables (i.e., rotational speed, clearance, angle of attack and camber of a NACA foil rotor) influence the pressure pulse at the screen plate surface. The numerical results were also compared to experimental measurements. This information provides a basic physical understanding of rotor performance and provides an experimentally validated computational tool for optimal rotor design.

## Literature Review

The pressure pulse generated by a foil rotor has been the subject of little published research. However, a few studies have given quantitative information about the effect of rotor design

<sup>1</sup>Now with Temec Engineering Group Ltd. Suite 375, 6450 Roberts St., Burnaby, BC, Canada, V5G 4E1

Contributed by the Fluids Engineering Division for publication in the JOURNAL OF FLUIDS ENGINEERING. Manuscript received by the Fluids Engineering Division August 11, 2003; revised manuscript received October 29, 2004. Review conducted by H. Johari.

parameters. The literature review given here represents the development of experimental and computational studies on rotor design in the pulp and paper industry.

Some experimental studies have been conducted to explain how screening performance is affected by the pressure pulse generated by the rotor. According to Niinimäki and Dahl [1], pressure pulses influence screening in two ways. First, the suction pressure pulses keep the screen apertures unplugged by disrupting the fiber mat and lifting the lodged particles away from apertures into the turbulent zone above the screen plate. Also, the suction pulses move a considerable amount of water and fines from the accept chamber back into the screen basket, and thus dilute pulp on the inner surface of the screen basket. According to Cox and Fredriksson [2], dewatering or thickening occurs during the phase of positive flow through the screen plate. This loss of water is compensated by filtrate recovered from the accept side of the screen basket by a long suction pulse. The amount of filtrate recovered can be controlled by the intensity and duration of the suction pulse.

Further experimental studies have been done on the factors that influence the shape and magnitude of the rotor pressure pulse and the effect of these pulse parameters on screen performance. Levis [3] studied the pressure pulse created by a foil-type rotor for screening of secondary fibers. He stated that the magnitude and shape of the pressure pulse were dependent on the foil shape, tip speed, and clearance between the foil and the screen cylinder. Levis suggested that as rotor speed was increased, the magnitude of the pressure pulse increased. Furthermore, he hypothesized that higher pulse magnitudes decreased the contaminant removal efficiency but increased the maximum capacity of the screen. He showed that a critical tip speed existed after which no further increase in capacity was achieved by increasing the rotor speed. Repo and Sundholm [4] investigated the effect of rotor speed on separation of coarse fibers in a pressure screen. Their experimental results indicated that decreasing rotor speed reduced the mass reject rate and improved separation efficiency compared to a higher speed. Gooding [5] measured the pressure pulse in an industrial Hooper PSV 2100 pulp screen. His results showed that increasing rotor speed strongly increased pulse strength. Although increased rotor speed shortened the duration of the pulse, the shape of the pulse was relatively unchanged. Increasing the speed of the rotor can consume significantly more power. Levis [3] found that the consumed power increased with rotor tip speed to the power of 2.5. Niinimäki [6] presented the power consumption measured at different rotor speeds and pulp consistencies. He showed that power consumption increased as rotating speed increased and consistency had only a small effect on power consumption.

Typical experimental studies on the effects of clearance and foil angle of attack were reported by Yu and DeFoe [7] and Niinimäki [6]. Yu and DeFoe [7] studied the pressure pulse signatures for a foil rotor and contoured drum rotor. The results of Yu and DeFoe showed a significant decrease in pulse magnitude for foil-type rotors when clearance increased. Niinimäki [6] reported the effects of clearance between the foil and screen surface on screen performance. As the clearance was reduced, the magnitude of the pulse increased, so screening efficiency decreased and capacity increased. He found that changes in foil angle of attack had a significant effect on screen performance. Furthermore, he showed that a greater angle of attack reduced the screening efficiency markedly with a corresponding increase in screen capacity. In addition, Niinimäki suggested that screen performance can be optimized by adjusting the foil angle of attack, especially if screening at higher consistencies.

The interaction between the fibers makes the flow behavior of pulp suspensions quite different from water. It was shown experimentally by Gonzalez [8] and Wikström [9] that the magnitude of pressure pulses decrease as the consistency increases.

A significant number of CFD studies examined the flow around a two-dimensional (2D) foil. Although there are still challenges

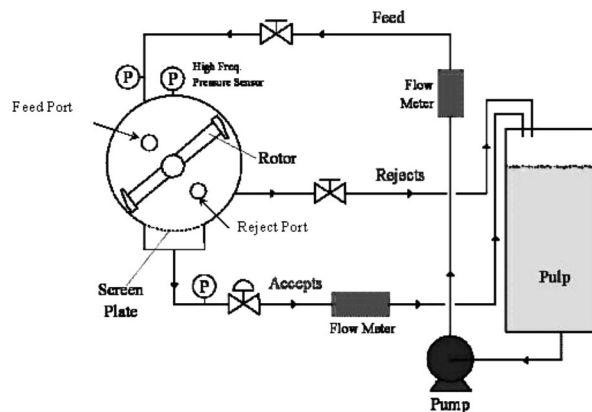


Fig. 1 Schematic diagram of cross-sectional screen

for CFD prediction of turbulent shear and separation, computations can generally predict surface pressures, velocity profiles, skin friction, lift, and drag with reasonably good accuracy at angles of attack below stall. Standard CFD methods provide reasonable prediction of flow variations with Reynolds numbers below stall, but predictions of when stall occurs are inconsistent and the skin friction predictions are often too high. Even with these limitations, CFD is a powerful technique for industrial equipment design and optimization.

Despite a rapid and substantial increase in the use of computer simulation in the pulp and paper industry in recent years, little CFD research has been done to study the pressure pulse generated by foil-type rotors. One useful study in this area was made by Karvinen and Halonen [10] who assessed rotor pressure pulsations using experimental and computational techniques. They found that the backflushing action of the pressure pulse was created by the acceleration of the flow through the gap between the moving rotor tip and stationary screen plate. This acceleration caused the local pressure on the feed side of the screen plate to decrease to the point that the flow through the aperture reversed. The flow then passed from the accept side of the screen plate to the feed side and released any plugged fibers. They used numerical methods to calculate the turbulent velocity field in a clearance between the rotating foil and screen basket and to simulate the pressure pulse generated in a screen. Their results showed that the foil shape greatly affected the form of pressure pulse. In addition, they found that the peak-to-peak pressure difference (maximum pressure minus minimum pressure) increased rapidly with increased rotational speed.

Marko and LaRiviere [11] used CFD software to model a 2D slice of an industrial pressure screen. Their results showed that the pressure pulse signatures had a reasonable correlation between the measurements and numerical predictions. It was found that mesh shape and density were very important to provide a good correlation with experimental results. Wikström [9] investigated the hydrodynamics inside a pulp screen using commercial CFD simulation software. Although the general flow behavior was captured well, pressure pulse data showed a deviation in absolute values when comparing simulations and experiments for water. CFD model overestimated the magnitude of pressure pulses, and simulation showed a delay in pressure drop at the beginning of the pulse.

None of the CFD studies on pressure-pulse generation included the detailed information required to evaluate the quality of the CFD analysis. Moreover, while several studies have compared foil shapes, none has examined a generic foil shape and considered how parameters affect flow patterns and the pressure pulse.

This work focuses on examining the pressure produced on the surface of a screen cylinder. We do not include the details of the cylinder because the geometry of the cylinder varies significantly

between manufacturers and applications. We consider a simple smooth surface to represent the cylinder. In addition, we assume that no flow is going through the cylinder for two reasons: (i) we consider the flow through the cylinder to be small with respect to the tangential velocity and (ii) we are specifically interested in the pressure that can be generated at the point where the cylinder is plugged with pulp fibers and there is no longer any fluid flow through the cylinder.

## Experimental Apparatus

The pressure pulses induced by foil rotors were measured for a wide range of design and operating variables. These measurements were of interest in their own right, but also served as a basis to validate the subsequent CFD solutions.

A laboratory cross sectional screen (CSS) was designed to simulate a slice of an industrial PSV 2100 pressure screen, as has been done in several experimental studies (e.g., [8,12–14]). Figure 1 shows a schematic of the flow loop and the principal components of this apparatus. The CSS test section has a diameter of 30 cm and depth of 5 cm. A 6 cm wide removable screen cylinder coupon is located in the bottom wall, with the remaining circumference a solid wall. The flow loop consists of a 150 l reservoir tank, a mixer, pump, two flow meters, two pressure transducers, valves, and PVC piping. A flow meter and pressure sensor are installed in both the feed and reject lines to monitor flow rate and pressure. The test fluid (in this study water) flows through a 25 mm diameter round pipe and flow meter and then enters the CSS through the feed port at the upper part of the CSS. Some of the suspension flows out through the openings of the slot coupon (i.e., the accept flow). The accept flow is approximately zero for this study. The rest (i.e., the reject flow) leaves the test section through the reject port and flows back to the reservoir tank.

A high-speed data acquisition system was used to record the form of the pressure pulsations. In particular, a high-frequency, 4 mm diameter pressure transducer was installed flush with the inside (feed) surface on the top wall of the CSS. This top wall represents the screen cylinder in an industrial pressure screen.

The pressure sensor was a strain-gage-based transducer with a specified accuracy of less than  $\pm 0.5\%$ . The pressure transducer was calibrated with a standardized static pressure calibrator to ensure the measurement bias is less than 0.5% of the maximum pressure. The measured pressure was fluctuating due to the turbulent motion of the fluid. The standard deviation is 3 kPa, which corresponds to a pressure coefficient fluctuation of 0.074 at the lowest rotor velocity of 9 m/s. To more accurately estimate the mean pressure profile, 120 pulses were averaged to provide a 95% confidence interval in the measured  $C_p$  of  $\pm 0.006$ .

An optical encoder, with a resolution of 2048 signals per revolution, was installed on the shaft of the rotor to precisely measure the position of the rotor. The rotary position sensor locates the position of the rotor to within an arc length of 0.5 mm. The resulting foil position is then  $\pm 0.25$  mm or in terms of chord length is  $\pm 0.625\%$  of chord for the 40 mm long foils used in this study. The position sensor is continuously recorded by the data acquisition system to provide a highly accurate rotational speed and foil tip speed. Tip speed is estimated to have an accuracy greater than  $\pm 0.1\%$ .

The CSS has been designed to measure the effect of some key operating and rotor design variables on screen performance and pulse generation. Figure 2 shows a schematic of the foil and defines the angle of attack and clearance. The rotor is driven by a 7.5 kW electric motor, controlled by a variable frequency drive. The gap between the outer wall and the foil was set using machine calipers and is extremely accurate. The estimate of the error is less than 0.05 mm. The accuracy of the measured angle of attack is estimated to be approximately  $\pm 0.1$  deg. Angle was also set using machined calipers.

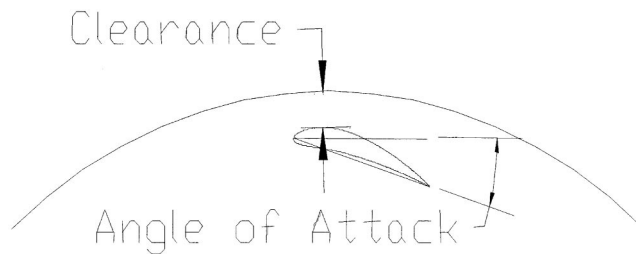


Fig. 2 Schematic of foil showing angle of attack and clearance

## CFD Model

CFD evaluations were conducted to extend and support the experimental measurements and to provide a more complete understanding of how some key rotor parameters affect the flow structures around the foil and the resulting pressure pulse profile. Numerical results were used to establish the relationship between the pressure pulse shape and rotor design and operating variables (e.g., rotating speed, angle of attack, foil clearance, and camber).

**Numerical Method.** The commercial code FLUENT 5.4 (Fluent Inc. [15]) was used for the numerical solution of the Navier-Stokes equations. The numerical method is based on a finite volume formulation applicable to structured grids. All variables, including velocity components and pressure, are averages applied to a control volume. A second-order spatial interpolation method was employed to obtain the velocity components and pressure on the control volume faces from those at the control volume centers. The control volume face values of the dependent variables are used to evaluate the convective fluxes.

Fluent's segregated steady-state solver was used for the numerical simulations. The numerical method is based on a multiblock, finite-volume formulation to solve the discretized Navier-Stokes equations in conjunction with the turbulence model. The SIMPLEC algorithm is used to couple pressure and velocity. A second-order upwind scheme was used for the space discretization of the convection terms in momentum and turbulence equations in all simulations. Also, a second-order accurate scheme was used to interpolate the pressure value on the control volume faces from those at the control volume centers in the momentum equations. The diffusion terms are approximated by a second-order accurate central-difference scheme. The stopping criteria for all calculations were when all residuals were below  $10^{-5}$ .

The standard  $k-\epsilon$  turbulence model is used for all calculations. Transport equations for  $k$ , the kinetic energy of turbulence, and  $\epsilon$ , the rate of dissipation, are solved together with the continuity and momentum equations.

**Mesh Generation.** Gambit, the meshing tool packaged with FLUENT CFD software, was used to generate a 2D multiblock mesh based on the surface information obtained from models of the experimental CSS apparatus. Figure 3 shows a structured multiblock grid typical of those used in this study. A C-mesh is used around the foil to provide good resolution around the leading edge of the foil, in the wake, and in the boundary layer. Because a logarithmic wall law is used to compute the skin friction coefficient, the first grid cell near the airfoil should be in the logarithmic region, i.e., the dimensionless distance to wall ( $y^+ = U_\tau y / \nu$ , where  $U_\tau$  is the friction velocity,  $y$  is the physical distance of the first centroid from the wall, and  $\nu$  is the kinematic viscosity) for the first cell center should be between 30 and 60. Near-wall mesh spacing was checked as a postprocessing step to ensure that this requirement was met. An  $H$  mesh is used up- and downstream of the foil to provide good mesh quality elsewhere.

**Boundary Conditions for Fluid Flow.** A rotating reference frame was used so that the flow was modeled in a coordinate system moving at the same speed as the rotating foil. In this case,

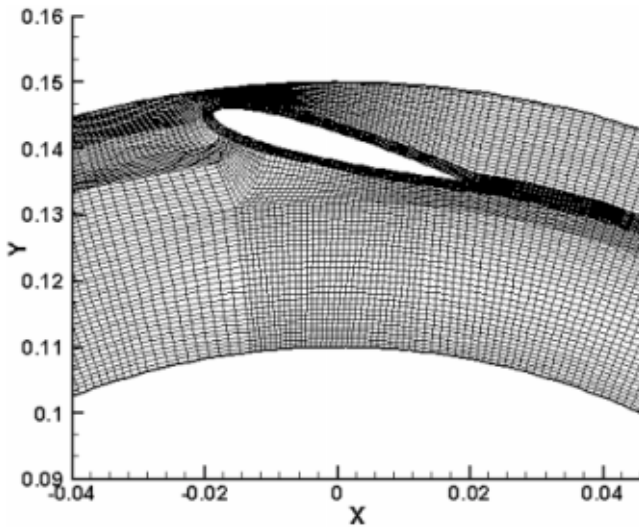


Fig. 3 Representative computational mesh

the flow was steady relative to the rotating frame. For the wall boundary conditions, the relative angular velocity was set to zero for the foil and inner wall, which moves at the speed of the rotating frame and, hence, are stationary in the rotating frame. The outer wall is stationary in the nonrotating frame of reference, therefore the velocity was set to zero in the absolute reference frame. If the wall velocities are specified in this manner, then only the rotating speed of the reference frame needs to be changed when there is a change in rotating speed of the foil.

The simplification of a rotating inner wall allows us to efficiently model the area of interest near the foil. The inner wall is not a physical wall but is a boundary that represents the portion of the fluid that rotates as a solid body with the rotor. We chose this boundary condition so that the fluid is rotating with the same rotational velocity as the rotor far from the cylinder (outer wall). This simplification allows us to only model the area of interest, around the foil near the wall.

Due to symmetry of the flow domain, calculations were performed for a sector of 180 deg (Fig. 4) and periodic boundary conditions were imposed in the circumferential directions at the two ends of the sector. The flow entering the computational model through one periodic plane was set identical to the flow exiting the domain through the opposite periodic plane.

**Model Validation.** The pressure pulsations are affected by the turbulence model used, especially for separated flows. Therefore, it is worth considering the errors in the  $k-\epsilon$  model for CFD study of pressure pulsation. Model validation was conducted by calcu-

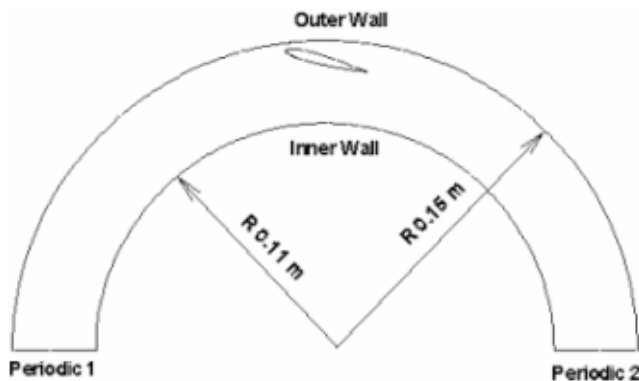


Fig. 4 Calculation domain and boundary conditions

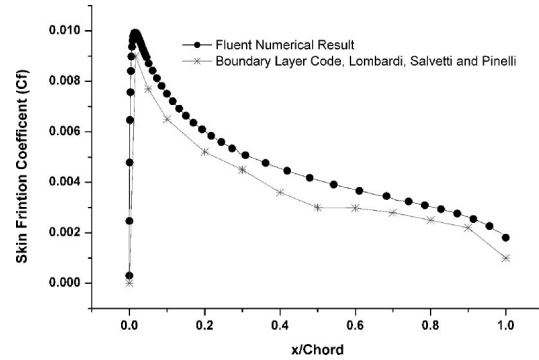


Fig. 5 Computed skin friction coefficient distributions over an NACA 0012 airfoil

lating the skin friction on a NACA 0012 (zero camber) airfoil in a straight channel at zero angle of attack for Reynolds number ( $Re$ , defined as  $Re = \rho Uc / \mu$ , where  $\rho$  is the density,  $U$  is the inlet velocity,  $c$  is the chord of the foil, and  $\mu$  is the dynamic viscosity) of  $3 \times 10^6$ . In Fig. 5, the local friction drag coefficient ( $C_f$ ) distribution obtained by the  $k-\epsilon$  model shows reasonable agreement (i.e., within 10%) with the numerical results calculated using a boundary layer code by Lombardi et al. [16]. The airfoil skin friction coefficient rapidly increases from a value of zero at the stagnation point to a peak value shortly downstream of the leading edge. This rapid increase is due to the rapidly increasing velocity as the flow external to the boundary layer rapidly expands around the leading edge. Beyond the peak,  $C_f$  monotonically decreases in the same qualitative manner as for a flat plate. The results for friction drag from the boundary layer code of Lombardi et al. [16] had been validated with experiment and were considered the baseline for accuracy. Based on this validation case of an airfoil, we have reasonable confidence in the predicted drag coefficient for attached flows.

For the configuration of interest in this study of a foil moving near a curved wall, a mesh refinement study has been conducted for the extreme cases of our test matrix. The pressure and velocity were shown to be independent of the number of cells used above the number used in this study.

## Results and Discussion

The pulse form for a range of rotor variables was examined using the aforementioned experimental measurements and CFD estimates. The technical characteristics and range of variables tested in the present experimental and numerical study and in industry applications are listed in Table 1.

The foil shape is defined by the NACA four-digit designation. The first digit defines the percent camber of the foil, the second digit defines the location of the camber in tenths of chord from the leading edge, and the last two digits define the thickness of the foil as a percent of chord (e.g., [17]).

The comparison of CFD predictions with the corresponding experimental measurements is valuable for the assessment of CFD simulations. It was found that although features and general trends of the pressure pulses were similar, the overall computed values of pressure pulse were 40–50% smaller than the measured values. The reason for the discrepancies might be that the 2D physical model used in the CFD study did not account the complex three-dimensional (3D) flow features in the experimental CSS. The presence of the side walls at the front and back of the CSS slows the rotational velocity of the fluid relative to the foil. The increased relative velocity would account for the higher experimentally measured pressure pulses than that calculated. In industrial pressure screens, there are no front and back walls to slow the fluid, and we would expect better correlation.

**Table 1 Technical characteristics and variables in present numerical and experimental study and in industry applications**

Characteristics and parameters	Present numerical and experimental study	Industry applications
Fluid	Water (20 °C)	Pulp suspension (60–90 °C)
Screen cylinder diameter	0.3 m	0.3–1 m
Foils	NACA 0012, 4312, and 8312, all with a chord length of 40 mm	Hooper etc., chord length from 30–80 mm
Rotor rotating speed	600, 800, 1000, 1200 and 1400 rpm	500–1000 rpm
Clearance between the foil and screen plate	2, 3, 4, and 5 mm	2–10 mm
Foil angle of attack	0, 5, 10, 15, and 20 deg	N/A

**Tip Speed.** Pressure pulses at the outer wall were calculated using CFD at five different rotational speeds for 0 deg angle of attack. The negative suction pressure peaks varied between 10 kPa at 600 rpm (tip speed=9.24 m/s) and 60 kPa at 1400 rpm (tip speed=21.55 m/s) for a NACA 0012 (zero camber) airfoil, as shown in Fig. 6. The magnitudes of both positive and negative pressure pulses increased with increased rotating speed for all the angles of attack studied. Pressure coefficient ( $C_p$ , defined as  $p/\frac{1}{2}\rho U_{tip}^2$ , where  $P$  is the pressure,  $\rho$  is the density, and  $U_{tip}$  is rotor tip speed) was obtained by normalizing the pressure with the dynamic pressure associated with the foil tip speed and fluid density. All the pressure curves in Fig. 6 collapsed into a single  $C_p$  curve, as shown in Fig. 7.

A comparison of the CFD and experimental results for the case of 0 deg angle of attack can be obtained by comparing the results of Figs. 7 and 8. The forms of the pressure pulses at the outer wall are similar, but CFD under predicts the  $C_p$  magnitude of the negative pulse by about 40%. Likewise, the agreement of the nondimensional pressure pulse form for a 20 deg angle of attack be-

tween the CFD calculation (Fig. 9) and measurements (Fig. 10) is good—but CFD estimates under predict the  $C_p$  magnitude of the suction pulse by 50%. The collapsed  $C_p$  curves in Figs. 7 and 9 indicate that magnitudes of positive and negative suction pressure pulse peak are proportional to the square of the tip velocity of the foil.

**Angle of Attack.** The variation of pressure distribution and flow pattern with angle of attack for a NACA 0012 foil are shown in Fig. 11. For a low angle of attack (<10 deg) the flow passes smoothly over the foil and is attached over most of the surface. However, as the angle of attack increases beyond 10 deg, the flow tends to separate from the top surface of the foil, creating a vortex that extends beyond the trailing edge of the foil, as shown by the streamlines in the figure. One consequence of the separated flow at high angles of attack is a large increase in pressure drag on the foil. Under these conditions, the increase in drag will increase the amount of power required to operate the rotor.

Figure 12 shows the calculated pressure pulse profiles on the screen cylinder surface for the NACA 0012 foil with five different angles of attack (0, 5, 10, 15, and 20 deg) at a constant clearance.

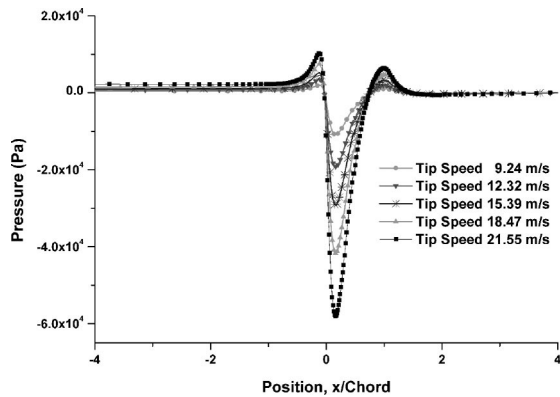


**Fig. 6 Numerical estimates of effect of rotating speed on pressure pulse (0 deg angle of attack constant gap)**

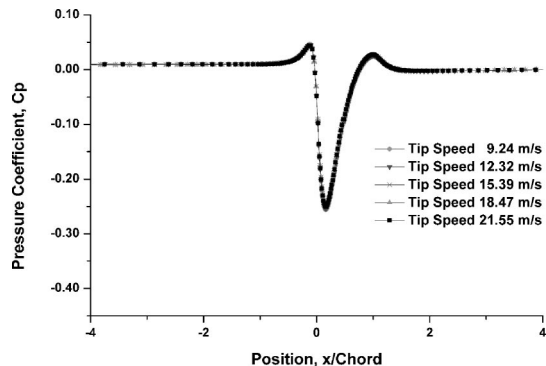


**Fig. 7 Numerical pressure coefficient versus position, x/Chord, (0 deg angle of attack constant gap)**

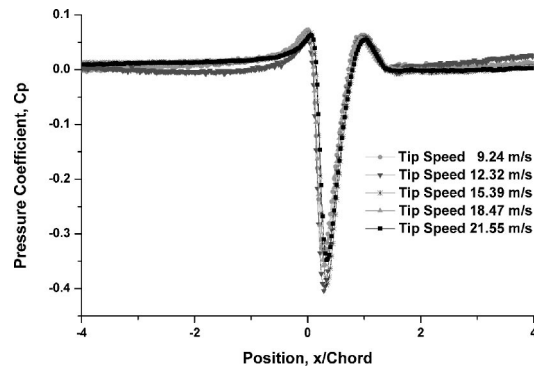


**Fig. 8 Experimental pressure coefficient versus position, x/Chord (0 deg angle of attack)**

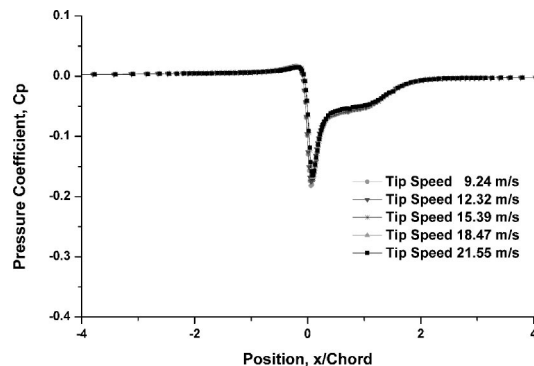


**Fig. 9 Numerical pressure coefficient versus position, x/Chord (20 deg angle of attack)**

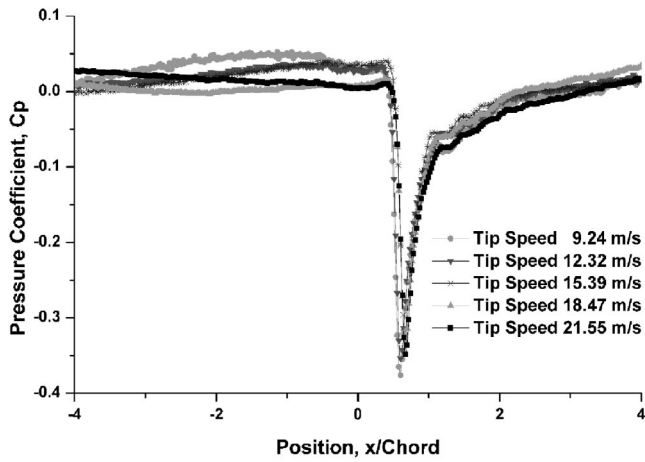


Fig. 10 Experimental pressure coefficient versus position,  $x/Chord$  (20 deg angle of attack)

The corresponding experimental results for the effect of angle of attack are shown in Fig. 13. There is a very good correspondence between the experimental measurements and numerical predictions for the form of the pulses and effect of changes in angle of attack. Both numerical results (Fig. 12) and experimental results (Fig. 13) show that a 5 deg angle of attack has the highest magnitude of negative suction pressure pulse. Both experimentally and computationally, the value of negative suction pulse peak for a 0 deg angle of attack falls between the values for a 15 and 20 deg angle of attack. As the angle of attack increases beyond 5 deg, the  $C_p$  magnitude of the negative suction pulse decreases

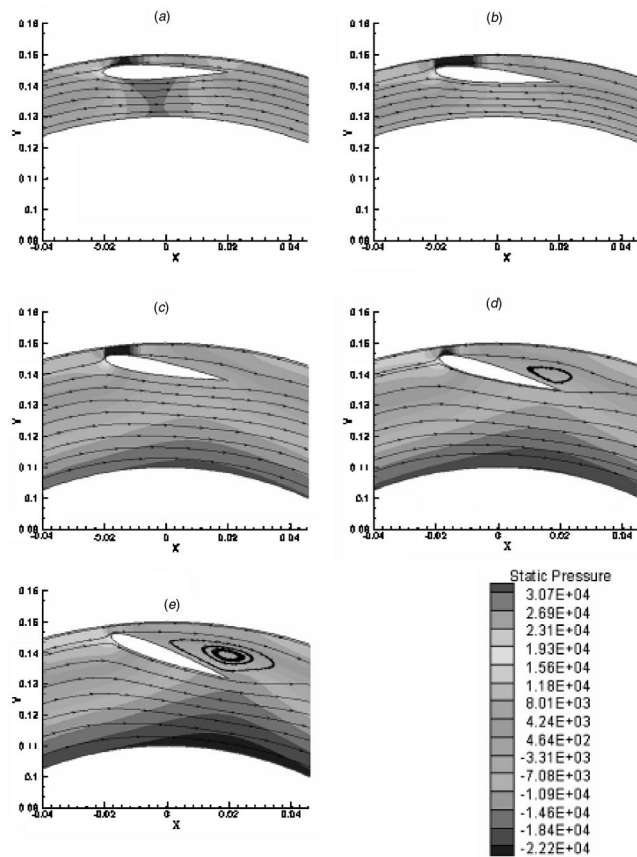


Fig. 11 Pressure contour and particle path lines. degree of attack (a)=0, (b)=5, (c)=10, (d)=15, and (e)=20

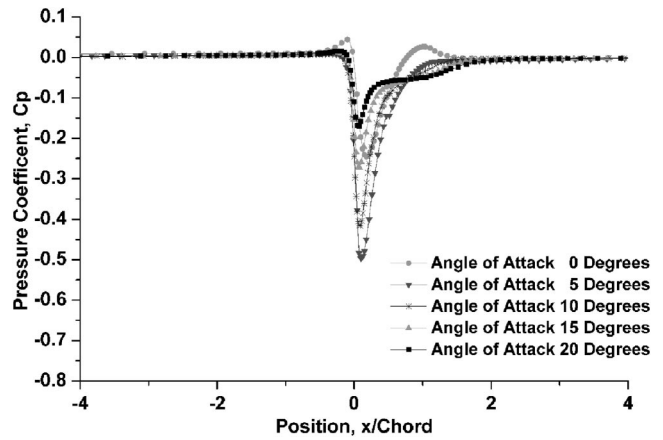


Fig. 12 Numerical pressure coefficient versus position,  $x/Chord$  for five different angles of attack

with increased angle of attack.

When the foil is at a nonzero angle of attack, greater than or equal to 5 deg, the positive pressure pulse at the leading and trailing edges of the foil are  $\sim 0$ . The positive pressure pulse is reduced for positive angles of attack because the stagnation point at the leading edge of the foil is located on the surface of the foil opposite to the screen cylinder and the foil effectively blocks the high-pressure region around the stagnation point from the cylinder. The resulting pressure pulse is flat with a sharp negative peak only in the vicinity of the foil. Reduction of the positive pressure pulse while maintaining a high negative pulse may significantly increase contaminant and fractionation efficiency of the screen by avoiding any tendency for the rotor to force contaminants through the apertures, while at the same time providing the strong back-flushing pulse that ensures good screen capacity.

Figures 12 (CFD) and 13 (experimental) both show a pressure plateau after the negative pressure peak for angles of attack  $> 15$  deg. This plateau would appear to be a result of flow separation from the upper surface of the foil. It is not clear that this aspect of the pulse form offers any particular benefit in the operation of the pulp screen rotor. What the above data do show is that the foil angle of attack has a strong effect on the shape and  $C_p$  magnitude of the pressure pulse and must be optimized for specific applications, especially if higher consistency screening is the desired purpose.

**Foil Clearance.** The clearance between the foil and screen cylinder may be adjusted in industrial screening applications to en-

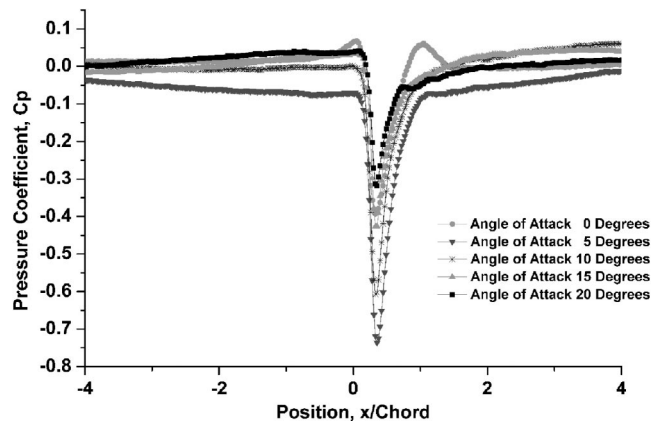


Fig. 13 Experimental pressure coefficient versus position,  $x/Chord$  for five different angles of attack

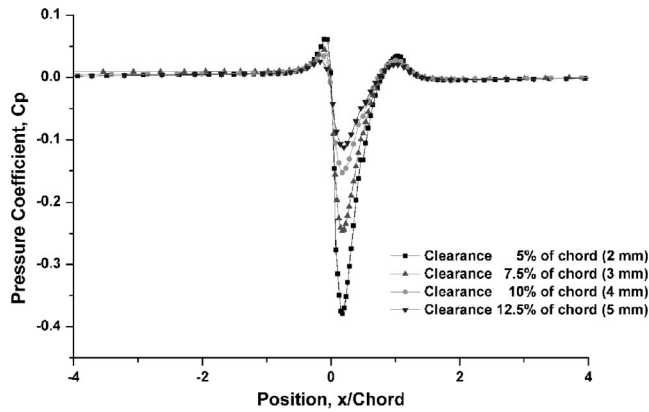


Fig. 14 Numerical pressure coefficient versus position,  $x/Chord$  for four different clearances (0 deg angle of attack)

hance the pressure pulsation. Pressure pulses for three different angles of attack (0, 5, and 20 deg) with a range of clearances 2–5 mm (5%, 7.5%, 10%, and 12.5% of chord) are shown in Figs. 14–16. Although increasing the clearance decreases the  $C_p$  magnitude of both the positive and negative pressure pulse peaks, it appears to have a stronger effect on the suction pressure peak. The tip speed is held constant at 18.47 m/s.

Figure 17 shows the  $C_p$  magnitude of the computed negative suction pressure peaks as a function of clearance for the range of angles of attack along with experimental results for the zero angle of attack. The experimental and computed peaks demonstrate the same trend: reducing the clearance increases the  $C_p$  magnitude of the negative pressure pulse. We also see that the foil at 5 deg angle of attack, which creates the greatest  $C_p$  magnitude of negative peak, is the most sensitive to variations in clearance.

Decreasing the clearance increases the  $C_p$  magnitude of the pressure pulse and the rotor's ability to clear plugged apertures. A smaller clearance also increases the probability of large contaminants becoming wedged between the cylinder and the rotor and potentially damaging the cylinder. For this reason, foil clearances are seldom below 2 mm.

**Foil Camber.** Classical aerodynamics theory predicts that a cambered airfoil will produce more lift than a noncambered airfoil at a given angle of attack. The same mechanism will result in a higher magnitude of negative pressure pulse on the screen cylinder. The degree of camber is the maximum distance between the mean camber line and the chord line in percent of chord. To determine the effect of foil camber on the  $C_p$  magnitude and shape

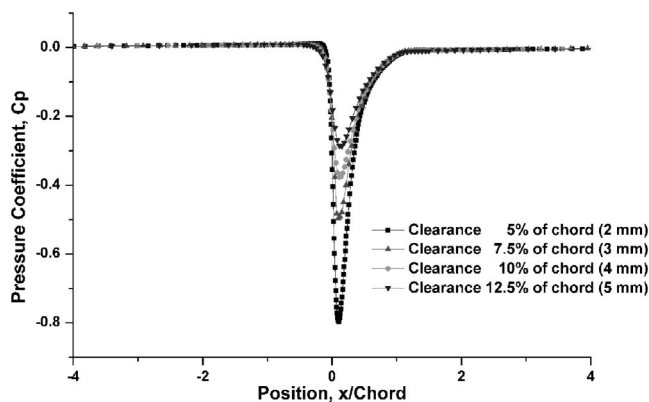


Fig. 15 Numerical pressure coefficient versus position,  $x/Chord$  for four different clearances (5 deg angle of attack)

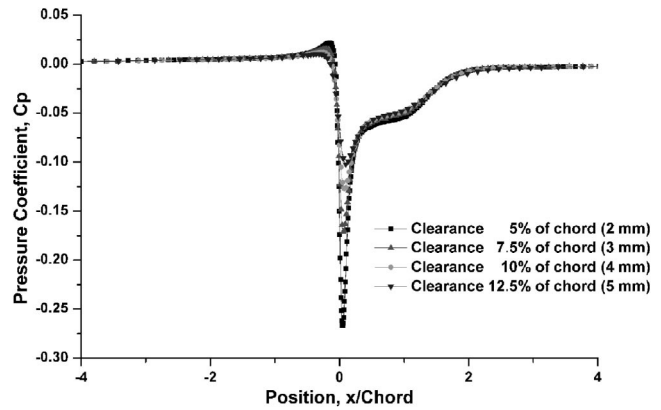


Fig. 16 Numerical pressure coefficient versus position,  $x/Chord$  for four different clearances (20 deg angle of attack)

of the rotor pressure pulse, numerical and experimental studies were conducted with NACA 0012 (no camber), NACA 4312 (4% camber), and NACA 8312 (8% camber) foils.

Figure 18 shows the numerically determined pressure pulses for the three airfoils with 0%, 4%, and 8% camber at 0 deg angle of attack. The increased camber increases both the  $C_p$  magnitude and width of the negative pressure pulse. Figure 19 shows the experimentally determined pressure pulses for the same three airfoils as Fig. 18 (0%, 4%, and 8% camber). The experimentally measured pressure pulses show the same increase in  $C_p$  magnitude and width as shown in the numerical results.

Figures 20 and 21 show the flow streamlines and pressure distribution for the NACA 4312 (4% camber) and NACA 8312 (8% camber) at five angles of attack equal to 0, 5, 10, 15, and 20 deg. The filled pressure contours show that the stagnation point progressively moves downstream of the leading edge over the bottom surface of the airfoil as the angle of attack is increased. This results in a decrease of the positive pressure pulse at the screen cylinder surface near the leading edge of the foil.

As foil camber is increased, the adverse pressure gradient on the foil surface facing the screen cylinder increases, and the flow separates at lower angles of attack. The stall angle of attack is  $\sim 5$  deg for NACA 8312,  $\sim 10$  deg for NACA 4312, and  $\sim 15$  deg for NACA 0012. More precise determination of the stall angle would require computation at intermediate angles of attack. The stalling phenomenon shown in Figs. 20 and 21 is termed “trailing-edge stall.” We see a progressive and gradual movement of separation from the trailing edge toward the leading edge as the angle

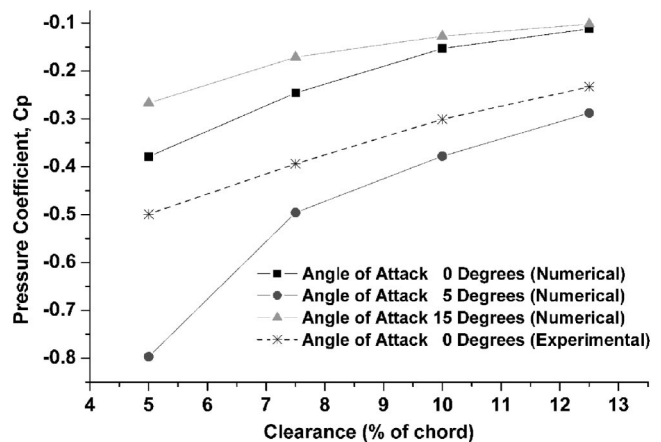


Fig. 17 Numerical and experimental suction pressure coefficient peak versus clearance for three different angles of attack

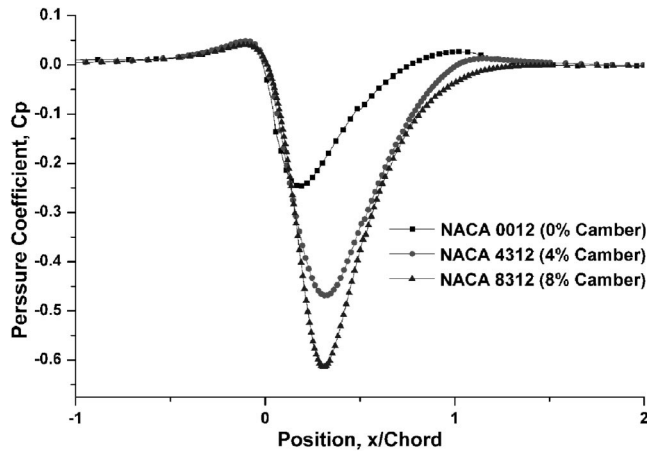


Fig. 18 Numerical pressure coefficient versus position ( $x/$ Chord) for 0 deg angle of attack

of attack is increased. The larger low-pressure region for cambered foils in the gap between the rotating foil and screen cylinder means that the width (or duration) of the negative pressure pulse is larger for cambered foils than for noncambered foils.

Figures 22 and 23 show the numerical and experimental pressure pulse profiles on the screen cylinder wall for a NACA 4312 foil with five different angles of attack (0, 5, 10, 15, and 20 deg). These figures show that 5 deg angle of attack has the highest negative suction pressure pulse and, thus, is expected to give the highest capacity. As the angle of attack increases beyond 5 deg, the  $C_p$  magnitude of the negative suction pulse decreases. The positive pressure peak near the leading edge of the foil is completely eliminated for foils operating at a positive angle of attack.

Figure 24 shows the computed pressure pulses at the screen cylinder for the NACA 8312 foil. This figure indicates that the  $C_p$  magnitude of the negative suction pulse decreases as the angle of attack increases due to the onset of separation. Thus for a NACA 8312 foil the maximum magnitude of pressure pulse occurs at 0 deg angle of attack.

Figure 25 shows the minimum pressure coefficients of the pressure pulses for the three cambers over all angles of attack for both the experimental and numerical results. The numerical and experimental  $C_p$  magnitudes of pressure pulse peak have the same trends. The  $C_p$  magnitudes of negative pressure peak obtained by experimental measurements are larger than the ones obtained by CFD calculations. There are substantial deviations of negative pulse peak for the NACA 4312 at 15 and 20 deg angle of attack

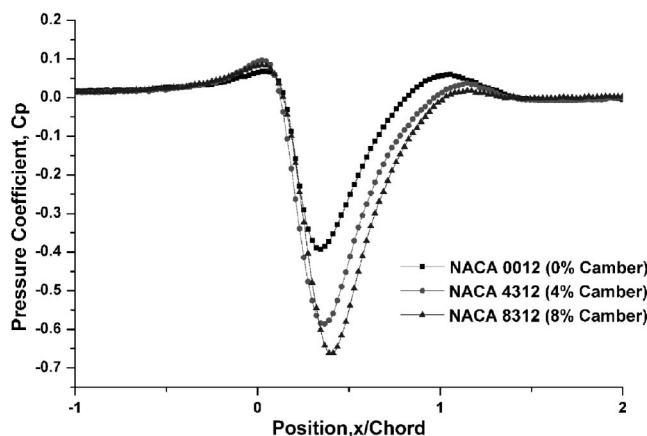


Fig. 19 Experimental pressure coefficient versus position ( $x/$ Chord) for 0 deg angle of attack

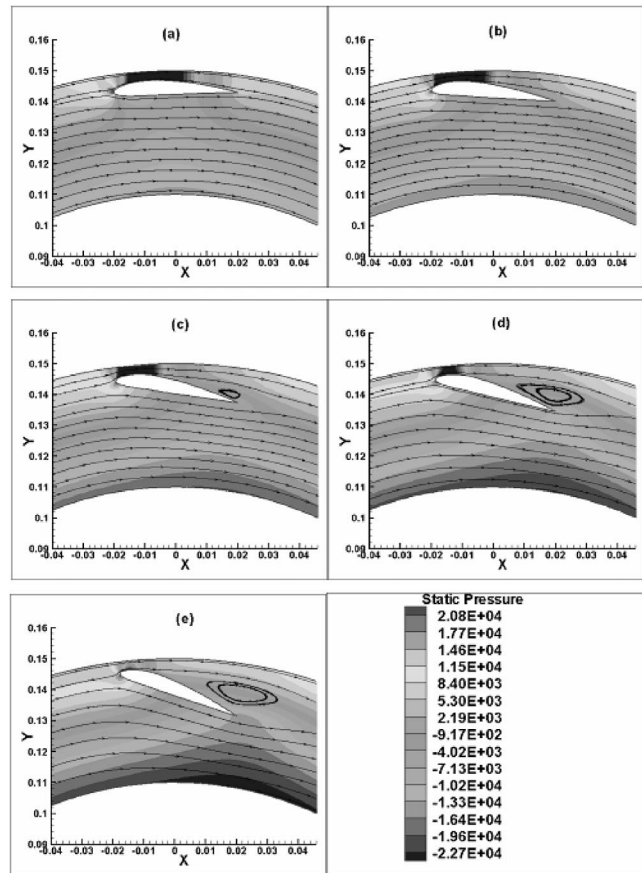


Fig. 20 Pressure contour and particle path lines for NACA 4312: degree of angle of attack (a)=0, (b)=5, (c)=10, (d)=15, and (e)=20

between CFD calculations and the experimental data. The reason for the discrepancy between the experimental and numerical pressure peaks for these two points is unknown.

For the three foils and five different angles of attack that were studied, the NACA 4312 (4% camber) at 5 deg angle of attack provided the highest magnitude of negative suction pulse peak. As angle of attack increased beyond 5 deg, the  $C_p$  magnitude of the negative suction pulse decreased with increased angle of attack. The largest negative peak for the NACA 8312 foil occurred at 0 deg angle of attack. This is because flow separation occurred at less than 5 deg angle of attack.

The ideal pulse form has not been established in the published literature. Intuitively, the negative pressure pulse magnitude and width would be the key parameters. Figure 26 shows that the negative pressure pulse width, defined as the width at half the negative pressure pulse, decreased as angle of attack increased for NACA 0012, 4312, and 8312 foils. The pulse widths for cambered foils were wider than that for noncambered foil.

The “normalized pulse strength” is proposed here as an alternate, and perhaps more effective, means of characterizing the effectiveness of a foil pulse. The normalized pulse strength is defined as the pulse width normalized by chord length multiplied by minimum pressure coefficient. Figure 27 shows that the normalized pulse strength for NACA 4312 at 5 deg and NACA 8312 at 0 deg had the highest value with almost the same magnitude.

## Discussion

The shape and magnitude of the rotor-induced pressure pulses are widely believed to have a fundamental effect on screen capacity, efficiency, and other key operating parameters. A positive

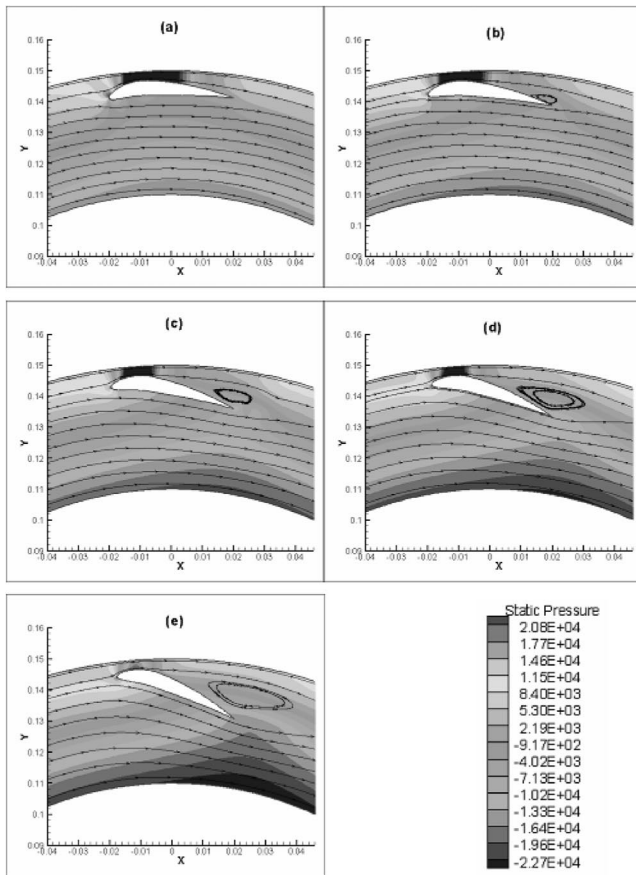


Fig. 21 Pressure contour and particle path lines for NACA 8312: degree of angle of attack (a)=0, (b)=5, (c)=10, (d)=15, and (e)=20

pressure pulse component is hypothesized to decrease the contaminant removal efficiency of the screen. This is because the high positive pressure pulse (found at the leading and trailing edge of the foil at 0 deg angle of attack) might force contaminants through narrow apertures. This might be especially true for flexible fibers

and deformable contaminant particles (such as “stickies”), which are adhesives found in recycled pulp. In this regard, the small or nonexistent positive pressure pulses generated by foils at nonzero angle of attack would be ideal for removing deformable contaminants.

The maximum achievable capacity is thought to be strongly correlated with the magnitude of the negative pressure pulse. The negative pulse reverses the flow through the apertures, backflushing the apertures and clearing particles lodged near the slot inlet and lifting them into the turbulent zone. As the peak strength increases, the suction pulse is more effective at clearing the screening apertures. Increasing the rotation speed will increase the pulse strength and the frequency of pulses. This correlation would be expected to exist only over a limited range, however, since too high a backflushing flow would reduce the net volumetric flow through the screen cylinder without producing any benefit.

Using a foil that produces a strong negative pressure peak provides the opportunity to reduce the total energy consumed by the rotor by providing a sufficient negative pulse at a low rotational speed. Ideally, the rotor speed would be set just high enough to meet the required capacity and runnability but no higher to minimize energy usage. Optimization of the rotational speed, clearance, angle of attack, and foil camber makes it possible to achieve increased efficiency at a reduced power consumption for each pulp type.

As discussed previously, the ability of the foil to remove pulp accumulation may be due to a combination of pulse height and width. For this reason, a “normalized pulse strength” term was defined as a combination of both width and magnitude of the pulse. The “performance” of the screen is indeed a composite of several indices, including capacity, efficiency, power, etc. Likewise the rotor produces several actions, including the backflushing duration, backflushing strength, pulp fluidization, rotational acceleration, etc. The interrelationships are typically nonlinear, and a single parameter is very unlikely to capture all of what is sought in “rotor performance.” However there may be composite parameters, such as normalized pulse strength, which more completely reflect the rotor action and facilitate rotor optimization. This will facilitate the conduct of more fundamental studies that seek to understand and optimize the form of the pressure pulse as a function of variables related to the shape and positioning of the rotor foil.

One should, of course, be cautious not to overstate the imme-

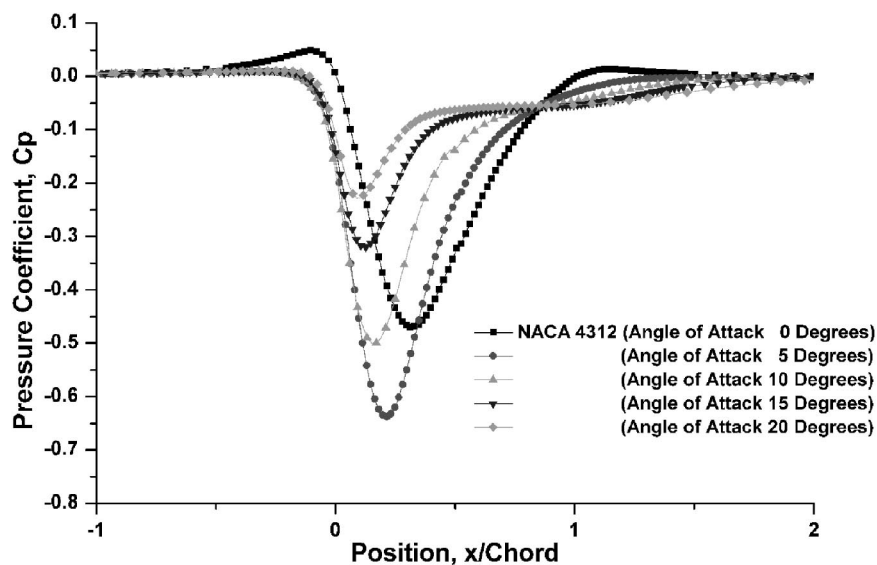


Fig. 22 Numerical pressure coefficient versus position ( $x/\text{Chord}$ ), NACA4312 (five angles of attack)

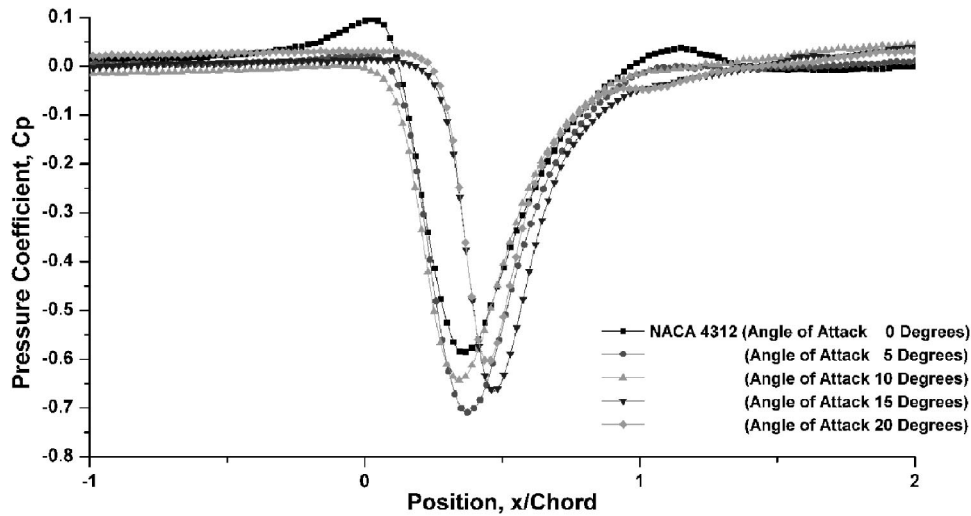


Fig. 23 Experimental pressure coefficient versus position ( $x/Chord$ ), NACA4312 (five angles of attack)

diate industrial impact of this study. The tests and simulation work shown above was made for water flows, not pulp. There are substantial differences in the character and behavior of these fluids. Likewise the lack of a clear model for what constitutes an “ideal” rotor pulse limits the immediate impact of this work. That said, this detailed study does point toward some clear opportunities for improvements in rotor design and for a better appreciation of the sensitivity of the pressure pulses to common rotor variables.

### Conclusions

Using both numerical and experimental approaches, the key design and operating variables affecting the pressure pulse on the surface of a pressure screen cylinder were investigated. Although the general pressure pulse signatures were captured well by the CFD model over a wide range of foil tip speed, clearance, angle of attack, and foil camber, comparison with experimental pressure pulse measurements showed deviations in  $C_p$  values by up to 50%.

Tip speed, angle of attack, clearance, and camber were all found to significantly affect the pressure pulse generated by the foil. In particular, it was shown that:

1. The magnitude of the pressure pulse peak increased linearly with the square of rotor tip speed for all angles of attack studied.
2. The maximum magnitude of negative pressure pulse occurred for the NACA 0012 and 4312 foils at 5 deg angle of attack and NACA 8312 at 0 deg. The positive pressure peak

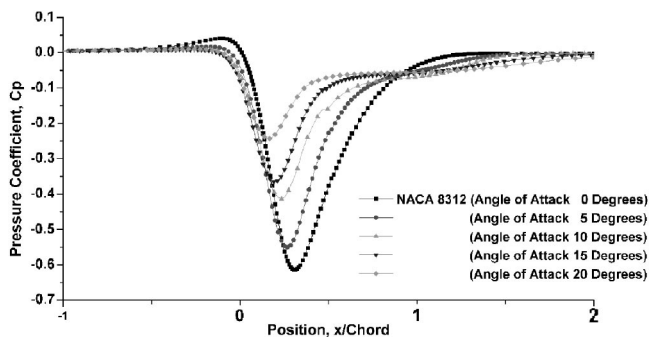


Fig. 24 Numerical pressure coefficient versus position ( $x/Chord$ ), NACA8312 (five angles of attack)

near the leading edge of the foil was completely eliminated for foils operating at greater or equal to 5 deg angle of attack.

3. The  $C_p$  magnitude of the negative pressure peak increased as clearance decreased.
4. The stall angle of attack was  $\sim 5$  deg for NACA 8312,  $\sim 10$  deg for NACA 4312, and  $\sim 15$  deg for NACA 0012. As the foil camber was increased, the flow separated at lower angles of attack because of the higher adverse pressure gradient on the foil surface near the screen cylinder.
5. The  $C_p$  magnitude and the width of the negative suction pulse increased with increased camber.

Most importantly, we have shown that CFD is an important tool for the optimal design and operation of rotors in industrial pressure screens.

### Acknowledgments

The financial and technical support of Advanced Fiber Technologies (AFT), the Pulp and Paper Research Institute of Canada

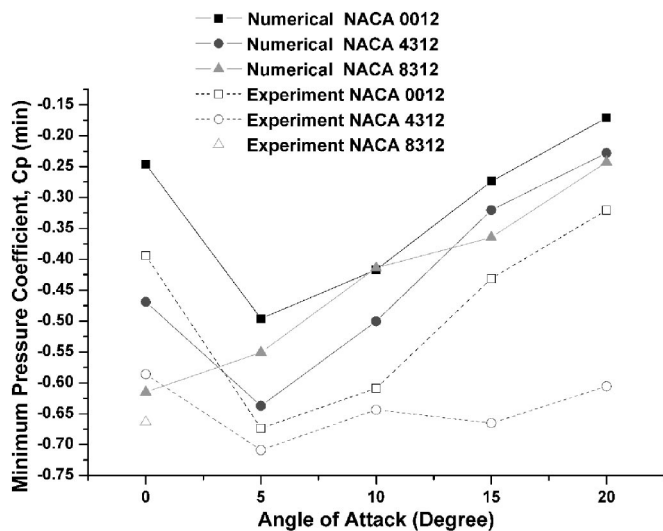


Fig. 25 Numerical and experimental minimum pressure coefficient versus angle of attack (deg)

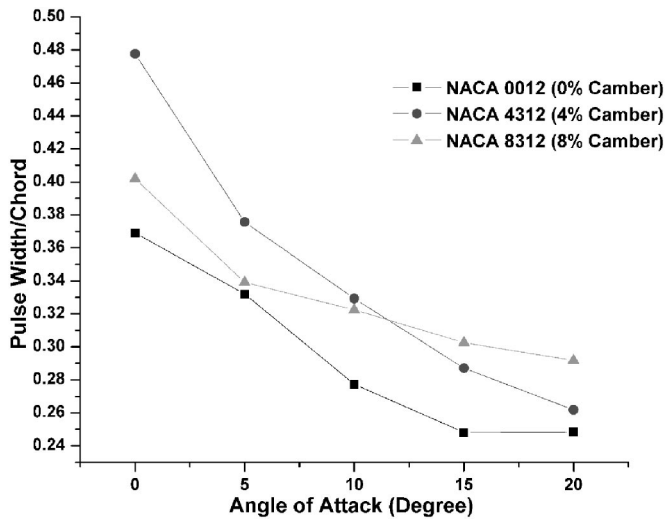


Fig. 26 Numerical pressure pulse width versus angle of attack

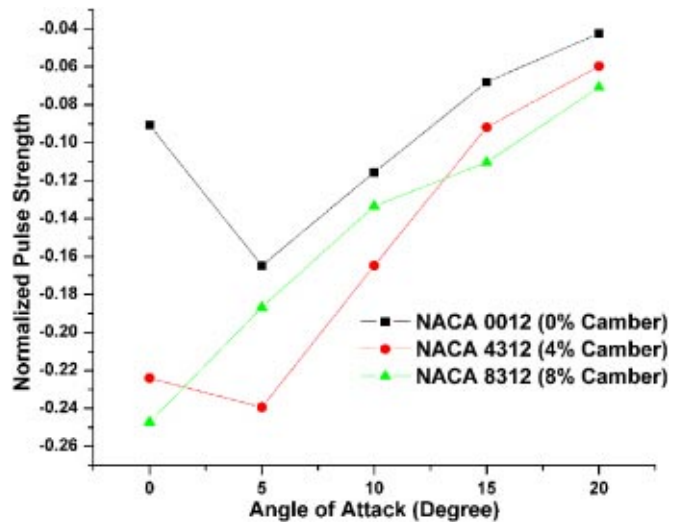


Fig. 27 Numerical normalized pressure pulse strength versus angle of attack

(Paprican), the Natural Sciences and Engineering Research Council of Canada (NSERC), and the UBC Advanced Papermaking Initiative (API) is gratefully acknowledged.

## References

- [1] Niinimäki, J., and Dahl, O., 1998, "A Comparison of Pressure Screen Baskets With Different Slot Widths and Profile Heights. Selection of the Right Surface for a Groundwood Application," *Pap. Puu*, **80**(8), pp. 31–45.
- [2] Cox, M., Fredriksson, B., and Koikkalainen, J., 2000, "Mill Experience With High-Consistency, Screening Technology for Recycled Fibre," *Pap. Technol. (Bury, U.K.)*, **41**(9), pp. 31–36.
- [3] Levis, S. H., 1991, "Screening of Secondary Fibers," *Prog. Pap. Recycl.*, **5**(1), pp. 31–45.
- [4] Repo, K., and Sundholm, J., 1996, "The Effect of Rotor Speed on the Separation of Coarse Fibres in Pressure Screening With Narrow Slots," *Pulp Pap. Can.*, **97**(7), pp. T253–T257.
- [5] Gooding, R. W., 1996, "Flow Resistance of Screen Plate Apertures," Ph.D. thesis, The University of British Columbia.
- [6] Niinimäki, J., 1999, "Phenomena Affecting the Efficiency of a Pressure Screen," *Tappi Pulping Conf.*, pp. 957–966.
- [7] Yu, C. J., and DeFoe, R. J., 1994, "Fundamental Study of Screening Hydraulics Part 3: Model for Calculating Effective Open Area," *Tappi J.*, **77**(9), pp. 125–131.
- [8] Gonzalez, J. A., 2002, "Characterization of Design Parameters for a Free Foil Rotor in a Pressure Screen," M.A.Sc. thesis, The University of British Columbia.
- [9] Wikström, T., 2002, "Transition Modelling of Pulp Suspensions Applied to a Pressure Screen," *J. Pulp Pap. Sci.*, **28**(11), pp. 374–378.
- [10] Karvinen, R., and Halonen, L., 1984, "The Effect of Various Factors on Pressure Pulsation of a Screen," *Pap. Puu*, **66**(2), pp. 80–83.
- [11] Marko, J. J., and LaRivière, C. J., 1999, "The Use of Computational Fluid Dynamics (CFD) in Pressure Screen Design," *Tappi Papermakers Conf.*, pp. 1477–1482.
- [12] Pinon, V., Gooding, R. W., and Olson, J. A., 2003, "Measurements of Pressure Pulses From a Solid Core Screen Rotor," *Tappi J.*, **2**(10), pp. 9–12.
- [13] Olson, J. A., and Wherrett, G. W., 1998, "A Model of Fibre Fractionation by Slotted Screen Apertures," *J. Pulp Pap. Sci.*, **24**(12), pp. 398–403.
- [14] Kumar, A., 1991, "Passage of Fibres Through Screen Apertures," Ph.D. thesis, The University of British Columbia.
- [15] Fluent Inc., 1998, *Fluent Users Guide*, Fluent Inc.
- [16] Lombardi, G., Salvetti, M. V., and Pinelli, d., 2000, "Numerical Evaluation of Airfoil Friction Drag," *J. Aircr.*, **37**(2), pp. 354–356.
- [17] Abbott, I. H., and Von Doenhoff, A. E., 1949, *Theory of Wing Sections*, McGraw-Hill, New York.